ACS APPLIED MATERIALS & INTERFACES

Research Article

www.acsami.org

Effect of Alcohol Treatment on the Performance of PTB7:$PC_{71}BM$ Bulk Heterojunction Solar Cells

Shuai Guo,[†] Biye Cao,[†] Weijia Wang,[†] Jean-François Moulin,[‡] and Peter Müller-Buschbaum*[,†]

[†]Physik-Department, Lehrstuhl für Funktionelle Materialien, Technische Universität München, James-Franck-Strasse 1, 85748 Garching, Germany

[‡]Helmholtz-Zentrum Geesthacht (FRM II), Lichtenbergstrasse 1, 85747 Garching, Germany

Supporting Information

ABSTRACT: The effect of an environmentally friendly alcohol treatment on bulk heterojunction (BHJ) polymer solar cells using the low-bandgap copolymer based on thieno[3,4-*b*]thiophene-*alt*-benzodithiophene units and [6,6]-phenyl-C71-butyric acid methyl ester is systematically investigated. Different alcohols are tested, and besides the most commonly used methanol treatment, other alcohols such as ethanol, 2-propanol, and 1-butanol also improve the device performance to certain extents as compared to the untreated solar cells. Changes of the surface structure caused by the alcohol treatment are probed with atomic force microscopy, and the modification of inner film morphology is probed by time-of-flight-grazing incidence small-angle neutron scattering (TOF-GISANS). UV/vis measurements show that the thickness of all BHJ films remains unchanged by the different solvent treatments. Thus, the enhanced device performance induced by the alcohol treatments is correlated to the reconstruction of the inner film structures probed with TOF-GISANS and the modified energy levels at the interfaces between the BHJ layer and the aluminum electrodes, evident by the enhanced short-circuit current and open-circuit voltage of the *I*−*V* curves.

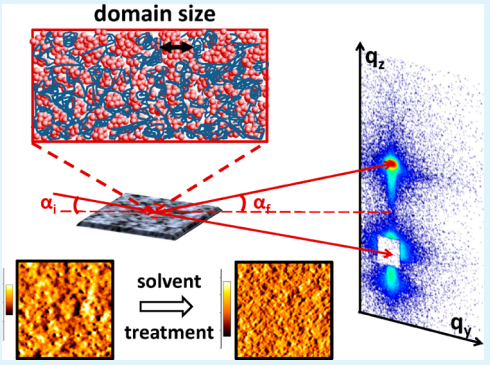

KEYWORDS: *polymer solar cells, alcohol treatment, power conversion efficiency, nanomorphology, GISANS*

1. INTRODUCTION

As an alternative renewable energy technology, polymer solar cells (PSCs) experienced compelling progress on the basis of device efficiency and lifetime in the past decades.[1−6] Although the power conversion efficiency (PCE) of traditional crystalline silicon has reached 25% with a typical lifetime of about 20 years and PSCs have achieved only PCE values of 12% with reported 7 year operating lifetimes, PSCs have promising advantages as compared to the traditional silicon solar cells such as mechanical flexibility and the use of lightweight materials.[5,7,8] Moreover, PSCs promise feasible cheap device fabrication costs and a rapid energy payback time.[9] However, to unlock the great potential of PSCs and to achieve a breakthrough in applications, further improvements of the device performance of PSCs are needed. Many approaches, such as the synthesis of new low-bandgap polymers, the introduction of solvent additives, the optimization of device geometry, post production treatments with thermal or vapor annealing, and interface engineering, have been examined.[10−14] To date, the highest published PCE of PSCs in a single junction device has reached 10%, above which commercialization is feasible.[15] Among the systems with high reported PCE values is a bulk heterojunction (BHJ) system which uses a low-bandgap copolymer based on thieno[3,4-*b*]thiophene-*alt*-benzodithiophene units (PTB7) and the fullerene derivate [6,6]-phenyl-C61 butyric acid methyl ester (PCBM) (e.g., reported PCE value is 9.2%).[15] In this type of system, PTB7:PCBM, solvent additives have shown to improve the efficiency of the PSCs considerably.[16,17] These solvent additives are generally small molecules, which are known to selectively dissolve the fullerene and to assist in forming the desired interpenetrating network-type morphology of the photoactive layer in the BHJ approach. For example, 1,8-diiodooctane (DIO) has shown to be a very successful solvent additive especially for PTB7:PCBM BHJ systems.[18] However, recently researchers have revealed that, although these small molecules indeed boost up the device performance of PSCs, the additive residues in the active layer of the fabricated devices due to its low volatility may adversely affect the device performance. As reported by Ye et al., the potential solvent additive residue limits the lifetime of such potentially higher efficiency devices.[19]

Several effective methods have been demonstrated to tackle the problem of residual processing additives, such as quick drying or slow drying and methanol treatment of the polymer blend thin films.[19] Among these approaches, the methanol treatment appears to be the most favorable strategy to remove the residual additives, as methanol is assumed to effectively remove the residual additives such as DIO and consequently improve the morphological stability. The low boiling point and

Received: November 12, 2014
Accepted: February 10, 2015
Published: February 10, 2015

DOI: 10.1021/am5079418
ACS Appl. Mater. Interfaces 2015, 7, 4641−4649

poor solubility (solubility <0.01 mg/mL) of methanol toward the organic materials present in the active layer make the post solvent treatment feasible. These results of Ye et al. are in agreement with a previous investigation by Zhou et al., who reported that efficiencies of PSCs as high as 7.9% have been achieved by the same methanol treatment procedure for the PTB7:[6,6]-phenyl-C_{71}-butyric acid methyl ester ($PC_{71}BM$) BHJ system.[20] Thus, the great potential, induced by the solvent treatment method for enhancing the efficiency of PSCs, is clearly evident.[21−24] The positive effect induced by methanol treatment for the PTB7:$PC_{71}BM$ BHJ system is attributed to an increased built-in voltage, a decreased series resistance, and a reduced charge recombination as reported by Zhou et al.[20] Moreover, Ye et al. claimed that the vacuum level on the metal side of the device is lifted by the methanol treatment, thereby reducing the electron injection barrier at the organic/metal interface and resulting in a better device performance.[19] So far all investigations about the impacts of methanol treatment have only addressed changes of the film surface of the active layer in PSCs and not that of inner structures. However, it is commonly recognized that the inner film morphology has a significant influence on the device performance.[25−27] Thus, a potential restructuring of the morphology inside the active layer induced by the solvent treatment is mostly neglected. Moreover, previous research was only focused on the well-working solvent methanol for enhancing device efficiency in PTB7:PCBM PSCs.[20] Investigations on the impacts of other alcohols, such as ethanol, 2-propanol, and 1-butanol, are still very limited.[28]

In the present investigation, we employ a variety of alcohols for post solvent treatment of the active layer of PSCs consisting of PTB7:$PC_{71}BM$ in a BHJ geometry to optimize the final device efficiency. We focus on examining the effect of different solvent treatments on the electronic properties of the solar cell devices and on the modification of the active layer morphology by comparing four alcohol treatments (methanol, ethanol, 2-propanol, and 1-butanol treatment). As the effect of solvent treatment using these four alcohols is investigated systematically for the first time, the main aim of this study is to track the trend of efficiencies of the solar cells obtained after different solvent treatments rather than fabricating novel record PSCs by fully optimizing the devices. After solvent treatment, the surface modifications of the polymer blend film are probed by atomic force microscopy (AFM), and the changes of inner film morphology are revealed by time-of-flight-grazing incidence small-angle neutron scattering (TOF-GISANS). To detect inner structures, diffuse scattering needs to be applied,[29,30] and the grazing incidence geometry has proven to be very well suited for this task.[31−34] Using neutrons instead of X-rays has the particular advantage that contrast conditions are improved in systems relevant for PSCs.[35,36] As a result of our investigation, the efficiency−morphology relationship is elucidated, and the reasons for the positive impact of solvent treatment on PTB7 based PSCs are suggested.

2. EXPERIMENTAL SECTION

2.1. Sample Preparation. Based on thieno[3,4-*b*]thiophene-*alt*-benzodithiophene units, low-bandgap copolymers PTB7 and [6,6]-phenyl-C71-butyric acid methyl ester ($PC_{71}BM$) were both purchased from 1-material. The solvent chlorobenzene and the alcohols methanol, ethanol, 2-propanol, and 1-butanol of above 99.8% purity were purchased from Carl Roth, and the additive 1,8-diiodooctane (DIO) from Sigma-Aldrich. All the materials and solvents were used as supplied. To prepare the solution, $PC_{71}BM$ was first dissolved in chlorobenzene and then added into PTB7. The weight ratio between PTB7 and $PC_{71}BM$ was 1:1.5, and the final solution concentration was 25 mg·mL^{-1}. In the end, 3 vol % solvent additive DIO was added into the blend solution. The solution was prepared in a nitrogen-filled glovebox. Due to the low solubility of the polymer PTB7, external heat (60 °C sand bath for 24 h) was used to obtain a well-dissolved solution and homogeneous photoactive layers afterward. Poly(3,4-ethylenedioxythiophene):poly(styrenesulfonate) (PEDOT:PSS) as received from Ossila Ltd. is a blend of two polymers, PEDOT and PSS, dispersed in H_2O. It was spin-coated as an ultrathin film and used as an electron blocking layer in the device. Films investigated by UV/vis spectroscopy were prepared on acid-cleaned transparent glass substrates. Films investigated with atomic force microscopy (AFM) and time-of-flight-grazing incidence small-angle neutron scattering (TOF-GISANS) were prepared on acid-cleaned and subsequently PEDOT:PSS-coated silicon substrates. For the TOF-GISANS investigation large silicon substrates with a size of (60 × 70) mm^2 were prepared due to the large footprint of the neutron beam. The corresponding solar cell devices were fabricated on ITO substrates purchased from SOLEMS with the size of (2.2 × 2.2) cm^2.

2.2. Device Fabrication. The simplest device configuration without a second hole-blocking layer or any optical spacer layers was adopted in our solar cells. The ITO substrates were partly covered by scotch tape and treated by chemical etching to remove the uncovered part. They were consecutively cleaned with alconox solution and several organic solvents in an ultrasonic bath (ethanol, acetone, and 2-propanol). PEDOT:PSS PH1000 water-based solution was first put in the same ultrasonic bath for breaking out large aggregated clusters and filtered by a PVDF filter with a pore size of 0.45 μm. After filtration, it was spin-coated with a rotation speed of 4000 rpm for 60 s. The obtained PEDOT:PSS films were dried at 150 °C for 10 min under ambient conditions, and premade PTB7:$PC_{71}BM$ blend solution was spin-coated with a rotation speed of 1000 rpm for 60 s in a nitrogen-filled glovebox. After the deposition of the photoactive layer, the solvent treatment procedure was directly applied to the samples: methanol (or other alcohol solvents) was deposited on top of the photoactive layer until the film surface was fully covered. The solvent was then subsequently spun off from the photoactive layer via spin coating at 2500 rpm for 40 s. All the solvent treatment procedures for the photoactive layer were performed in the same glovebox. Finally, the samples were shifted to an evaporation chamber, and a layer of aluminum under vacuum conditions (3.0 × 10^{-5} mbar) was deposited by thermal evaporation to complete the solar cell fabrication. The rate of aluminum deposition was monitored by a quartz crystal rate meter purchased from Inficon. The deposition rate was started at 0.1 Å·s^{-1} and speeded up to 20 Å·s^{-1} at the highest. The evaporation was manually stopped when the aluminum film thickness reached 100 nm.

The solar cell performance was characterized under standard 1000 W·m^{-2} AM 1.5 G illumination. The simulated solar spectrum was always precalibrated by a calibration cell made of monocrystalline silicon purchased from Fraunhofer ISE. The corresponding $I-V$ curves were recorded with a source meter (Keithley 2400) with 200 points in the range from −1 to 1 V. The effective area of the diode was on the order of 13 mm^2, and the precise values for efficiency calculation were individually determined for each pixel with the assistance of optical microscopy. More than 200 devices were fabricated and measured.

2.3. Device and Active Layer Characterization. Absorption measurements were performed with a UV/vis spectrometer (Lambda35, PerkinElmer) in transmission geometry. The transmitted signals were recorded in the wavelength range between 300 and 850 nm.

Atomic force microscopy (AFM) was used to obtain topography and error images of the film surfaces. All the samples were measured in tapping mode at different positions with different scan sizes to verify the homogeneity of the films. The software Proscan Image Processing (Park Scientific Instruments) was used to process the obtained AFM images and to avoid deviations from the real film thickness.

Time-of-flight-grazing incidence small-angle neutron scattering (TOF-GISANS) measurements were performed at the Forschungs-Neutronenquelle Heinz Maier-Leibnitz (FRM II) in Garching,

DOI: 10.1021/am5079418
ACS Appl. Mater. Interfaces 2015, 7, 4641−4649

Germany. A neutron beam with variable wavelengths from 2 to 20 Å was used with a resolution of 10%. The sample−detector distance was set to 10.5 m to obtain a reasonable q_y range. A multiwire 2D detector made of ^{3}He with an active area of 500 mm^2 was used to record the scattered neutron signals. The ^{3}He detector had (200 × 200) pixels with a pixel size of (2.92 × 2.92) mm^2. A double-chopper system with the required rotation speed was used to define the neutron pulses. By varying the wavelength of the neutrons instead of varying the incident angles, the TOF-GISANS measurements provided direct information covering a large q range with full penetration of the film from a single incident angle α_i = 0.45°. To get precise structure information, vertical and horizontal line cuts (and the corresponding modeling) of the 2D GISANS data were performed (referring to the sample surface) as described in the main text.

3. RESULTS AND DISCUSSION

3.1. Current−Voltage Characterization. The photovoltaic performance of pristine PTB7:PC$_{71}$BM BHJ solar cells is compared with that of solvent-treated solar cells using four different alcohols. More than 200 individual devices were fabricated, and the I−V curves of these devices were measured and analyzed. In order to gain fundamental insights in the efficiency−morphology relationship, we have chosen the simplest device configuration so that the unexpected non-morphological reasons can be ruled out. A second hole-blocking layer or optical spacer layers are also neglected. The realized PSCs use a functional stack which consists of indium tin oxide (ITO)/poly(3,4-ethylenedioxythiophene):poly-(styrenesulfonate) (PEDOT:PSS)/PTB7:PC$_{71}$BM/aluminum (Al). Moreover, a relatively large solar cell pixel size (13 mm^2 in this work as compared with 4.5 mm^2 in the investigation by Zhou et al.) is used in our study.[20] Therefore, slightly lower values of the device efficiency as compared to the reported results are reasonable. Besides the recently published methanol treatment route, the use of other alcohols (ethanol, 2-propanol, and 1-butanol treatment after the deposition of the photoactive layer) is also found to be able to improve the efficiency of PTB7:PC$_{71}$BM BHJ solar cells to a certain extent. The measured I−V curves of the reference PTB7:PC$_{71}$BM polymer BHJ solar cell and counterparts with additional alcohol treatments are presented in Figure 1.

It can be observed that simultaneous improvements of the short-circuit current density J_{sc}, the open-circuit voltage V_{oc}, and the fill factor FF are obtained by these alcohol treatments. However, the efficiency improvement does not exhibit a simple relationship with the used alcohols' properties, such as the number of carbon atoms or the vapor pressure of certain alcohol. Methanol treatment gives rise to the highest efficiency, whereas the ethanol treatment presents the most moderate enhancement of the device performance.

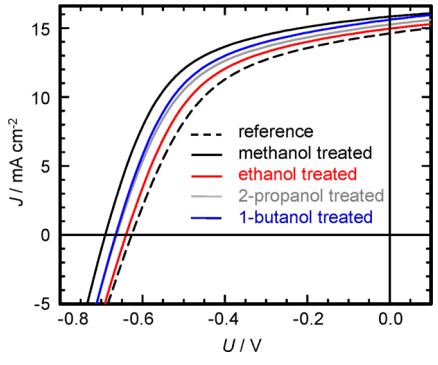

Figure 1. I−V curves of PTB7:PC$_{71}$BM BHJ solar cells without (dashed line) and with post solvent treatment (solid lines) using methanol (black), ethanol (red), 2-propanol (gray), and 1-butanol (blue), measured under illumination with 1000 W·m^{-2} (air mass AM 1.5G spectrum).

In order to obtain a comparison, the corresponding cell parameters J_{sc}, V_{oc}, and FF are listed in Table 1. The PCE of the polymer solar cells in a conventional device structure increases from 4.5 ± 0.1% to a maximum of 6.0 ± 0.1% for methanol-treated devices, whereas ethanol-treated devices only achieve 4.9 ± 0.2%. As for solar cell devices with 2-propanol and 1-butanol treatment, the PCEs improve up to 5.2 ± 0.2% and 5.4 ± 0.2%, respectively. As mentioned above, solvent treatment leads to a simultaneous improvement of J_{sc}, V_{oc}, and FF in general.

Table 1. Average Characteristic Parameters of PTB7:PC$_{71}$BM BHJ Solar Cells without and with Post Solvent Treatment Using Methanol, Ethanol, 2-Propanol, and 1-Butanol Measured under Illumination with 1000 W·m^{-2} (AM 1.5 G)

sample	J_{sc} (mA/cm^2)	V_{oc} (V)	FF (%)	PCE (%)
reference	14.58 ± 0.3	−0.62 ± 0.01	50 ± 1	4.5 ± 0.1
methanol	15.75 ± 0.1	−0.69 ± 0.01	55 ± 1	6.0 ± 0.1
ethanol	15.00 ± 0.1	−0.63 ± 0.01	52 ± 1	4.9 ± 0.2
2-propanol	15.32 ± 0.1	−0.66 ± 0.01	52 ± 1	5.2 ± 0.2
1-butanol	15.60 ± 0.1	−0.66 ± 0.01	53 ± 1	5.4 ± 0.2

The improvement of the final device performance is mainly ascribed to the enhanced V_{oc} and FF introduced by the solvent treatment: For methanol-treated devices, a significant increase of V_{oc} from 0.62 ± 0.01 V to 0.69 ± 0.01 V is achieved, and FF also shows a decent enhancement from 50% up to 55%. Similarly, a relatively moderate increase of V_{oc} (up to 0.66 ± 0.01 V) and FF (up to about 52 ± 1%) is observed for both 2-propanol- and 1-butanol-treated devices. The increase of V_{oc} (0.63 ± 0.01 V) and FF (52 ± 1%) for ethanol-treated devices is the lowest. In comparison, only the increase of J_{sc} is moderate, irrespective of the used alcohol, which indicates that the charge mobility is not dramatically affected by the alcohol treatment. Further optimizations of the device performance can be realized for instance by an incorporation of spacer layers between the photoactive layer and the Al electrode or by having the complete device fabrication and measurement procedures under nitrogen atmosphere.[20,23] However, the implementation of spacer layers is very time-consuming and challenging due to the complexity of multilayer devices, which adds an unnecessary degree of complexity to the investigation of the film structure. Moreover, a meticulous selection of the interlayer material is additionally required in order to perfectly match the highest occupied molecular orbital (HOMO) value of the donor material and the lowest unoccupied molecular orbital (LUMO) value of the acceptor material. In comparison, alcohol treatment, with which we can achieve comparable results, appears to be a much more efficient method of improving the efficiency of PSCs without time-consuming and laborious fabrication procedures. Since we mainly focus on understanding the significant positive effect of post solvent treatment, our results are sufficient to provide first insight on further investigation onf the efficiency−morphology relationship.

DOI: 10.1021/am5079418
ACS Appl. Mater. Interfaces 2015, 7, 4641−4649

3.2. Absorption Characterization. From the UV/vis measurements (see Figure 2), a linear superposition of the

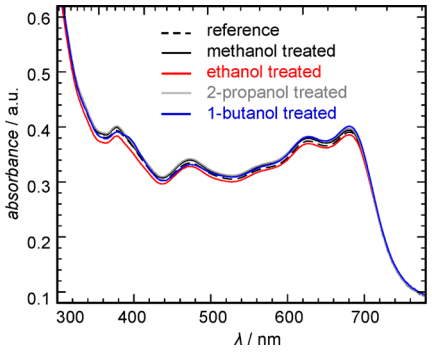

Figure 2. Absorption spectrum of PTB7:$PC_{71}BM$ BHJ active layers without (dashed lines) and with postsolvent treatment (solid lines) with methanol (black), ethanol (red), 2-propanol (gray), and 1-butanol (blue).

spectra of the individual materials, the fullerene $PC_{71}BM$ and the polymer PTB7, is observed to successfully explain the measured data. For pristine (dashed curve) and alcohol-treated PTB7:$PC_{71}BM$ BHJ films (solid curves), the absorption spectra are identical. According to the Beer–Lambert law, the absorption is proportional to the film thickness, if the same material composition is used. Hence, it is concluded that the solvent treatment with the four different alcohols causes no evident change in the film thickness, which is in agreement with Zhou's findings as verified by profilometry.[20] Moreover, the characteristic shape of the absorption spectra remains unchanged, which implies that the crystallinity is not affected by the alcohol treatment. These observations show that the optical properties of the components of the blend are not altered by the alcohol treatments. Hence, it rules out the possibility that the difference among device performances of the pristine and the solvent-treated PTB7:$PC_{71}BM$ BHJ solar cells is caused by the change of the film thickness or crystallinity and consequent change in the light absorption of each film. The performance enhancement must arise from either the reconstructed morphologies of the PTB7:$PC_{71}BM$ active layers or the modified interface energy levels, which is discussed in the following.

3.3. Mesoscopic Surface Structures of Active Layers. Since the photovoltaic performance of PSCs is significantly determined by the morphology of the photoactive layer,[25,26,37] we study the morphology of the surface of the PTB7:$PC_{71}BM$ films without and with solvent treatment using optical microscopy and AFM. Optical micrographs show homogeneous film surfaces for all investigated samples (see Figure S1, Supporting Information). In order to further resolve smaller surface structures and to determine the surface roughness of the films down to nanometer length scale, AFM measurements are performed in tapping mode. The topography images of pristine and solvent-treated PTB7:$PC_{71}BM$ films are shown in Supporting Information Figure S2 . Both the pristine and solvent-treated PTB7:$PC_{71}BM$ films exhibit similar surface topographies, irrespective of the used alcohols. Thus, regarding the film surface topography, homogeneous films are observed down to the nanometer level without serious impact of the used alcohols. The surface roughness values measured from the topography images are ~12 Å for pristine blend films as well as for methanol- and ethanol-treated films. The roughness of the active layers slightly increases up to ~14 Å for 2-propanol- and 1-butanol-treated films. Thus, the PTB7:$PC_{71}BM$ film roughness stays rather constant before and after solvent treatment.

However, AFM error images of pristine and solvent-treated PTB7:$PC_{71}BM$ films reveal small differences in the surface structures (see Figure 3). A phase-separated morphology is

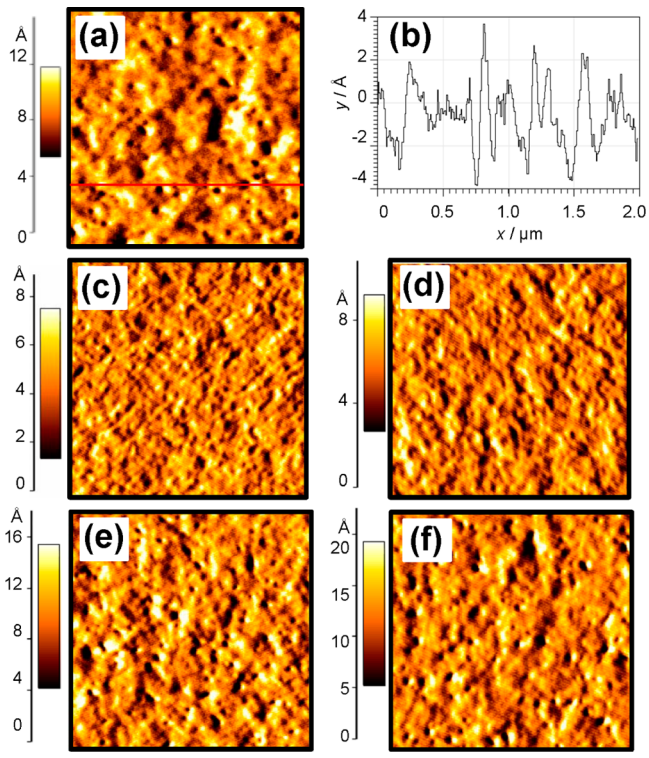

Figure 3. AFM error images (scan size 2 × 2 μm^2) of PTB7:$PC_{71}BM$ films: (a) pristine film without any solvent treatment, (b) the corresponding line cut profile of the pristine film at the position indicated by the red line, (c) methanol-treated, (d) ethanol-treated, (e) 2-propanol-treated, and (f) 1-butanol-treated. Different color bars are used for illustrating the height variation.

observed in general for all preparation procedures, in which details in the morphology depend on the sample treatment: A phase separation structure with coarsened domains is formed for pristine PTB7:$PC_{71}BM$ films, whereas smaller structures are generally observed for all films after alcohol treatment. Among all, the smallest structure sizes are obtained from methanol-treated films, which is in good agreement with previous investigations by Wang et al.[28] Such smallest structure sizes match well with the highest solar cell efficiency found for the methanol treatment. Since AFM measurements provide only a direct image of the film surface morphology, no quantitative results regarding the modification of the inner film morphology can be obtained from such technique. To further explore the morphological evolution induced by solvent treatment within the films, advanced scattering techniques are applied to gain statistically relevant structure information.

3.4. Mesoscopic Inner Lateral Structures of Active Layers. In this work, diffuse scattering in grazing incidence geometry is used to detect lateral structures of the active layers.[26,38,39] Grazing incidence small-angle neutron scattering (GISANS) is applied to obtain information about the inner nanoscale structures, such as characteristic lateral length scales, domain geometries, and size distributions.[34,40] The GISANS

DOI: 10.1021/am5079418
ACS Appl. Mater. Interfaces 2015, 7, 4641–4649

experiments are performed in time-of-flight (TOF) mode, which uses a broad neutron wavelength range instead of a fixed value. TOF-GISANS has proven its ability to probe depth-sensitive information from the film volume based on different neutron wavelengths; i.e., the structural information from the bulk film is probed at short neutron wavelengths, whereas surface sensitive information is obtained using long neutron wavelengths.[41−43]

In Figure 4 several representative two-dimensional (2D) GISANS data of the pristine PTB7:$PC_{71}BM$ film (Figure 4a−d)

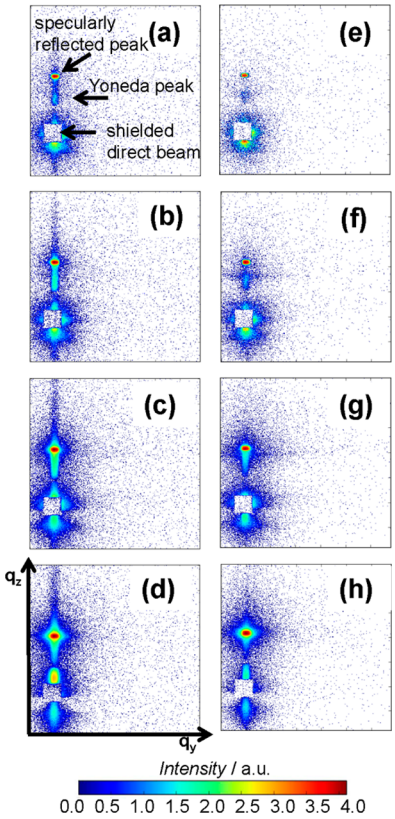

Figure 4. Example of 2D GISANS data of the pristine PTB7:$PC_{71}BM$ film (a−d) and 1-butanol-treated PTB7:$PC_{71}BM$ film (e−h) obtained simultaneously in the TOF-GISANS measurement. From top to bottom, the corresponding mean wavelengths are 3.25, 4.25, 6.25, and 9.25 Å, respectively.

are shown compared with the 1-butanol-treated PTB7:$PC_{71}BM$ film (Figure 4e−h). From the broad wavelength band we have selected four wavelengths (3.25, 4.25, 6.25, and 9.25 Å) in this graph, which were all measured simultaneously in the TOF-GISANS measurement. Three main features are observed in these 2D GISANS data (from top to bottom for each GISANS image): the specularly reflected peak, the intensity side maxima at the Yoneda peak position, and the transmitted signal centered on the shielded direct beam. For the 2D GISANS data obtained from the pristine PTB7:$PC_{71}BM$ film shown in Figure 4a−d, no obvious changes can be observed with the increase of wavelength except the variation of the intensity, which only originates from the wavelength distribution of the incoming neutron flux. In comparison, the GISANS data of the 1-butanol-treated PTB7:$PC_{71}BM$ film shown in Figure 4 (e−h) exhibits more pronounced intensity side maxima at the Yoneda peak position. Moreover, these side maxima expand to high q_y values, indicating that a decreased prominent length scale is obtained after 1-butanol treatment. In addition, the intensity side maxima in Figure 4e−h first expand to a high-q_y range at low neutron wavelengths (range from 3.25 to 6.25 Å) and then diminish at long neutron wavelengths (above 9.25 Å), which further implies that the average domain size on the film surface is bigger than that of the inner film.

In order to obtain quantitative structure information, vertical and horizontal line cuts of the 2D TOF-GISANS data are performed (referring to the sample surface).[44] The vertical line cuts of pristine and solvent-treated PTB7:$PC_{71}BM$ films are shown in Supporting Information Figure S3. In general, one can obtain structural information from the analysis of such vertical line cuts (referring to sample surface). From the vertical line cuts shown in Supporting Information Figure S3, pronounced specular peaks and a shift of the Yoneda peak toward larger exit angles (as indicated by the arrow in Supporting Information Figure S3) are observed. The shift of the Yoneda peak position can be explained by the relation between the critical angle (which determines the position of the Yoneda peak) and the neutron wavelengths according to the equation $\alpha_i = \lambda\sqrt{(SLD/\pi)}$.[45] Therefore, the shift of the Yoneda peak position is caused by the increase of the neutron wavelength. It should be noted that the shift of the Yoneda peak observed in the vertical line cuts does not contradict with the inconspicuous shift seen in the 2D GISANS data shown in Figure 4, as each 2D GISANS image covers a different q_{yz} range. The detected angle α_f exhibits a linear dependence on the wavelength, as summarized in Figure S4 (Supporting Information).

Since the horizontal line cuts at the critical angle of each material contain the information about the lateral structures,[44] we focus on these line cuts to determine the domain sizes and furthermore the size distribution. The horizontal line cuts are plotted in Figure 5 for all 2D GISANS data obtained from the pristine and the solvent-treated films. In Figure 5 the neutron wavelength increases from 5.25 Å (bottom, red data points) to 10.75 Å (top, green data points) with an increment of 0.5 Å. As explained above, the morphology of the bulk film is revealed at short wavelengths (smaller than 8 Å at our chosen parameters) and the surface sensitive information at long neutron wavelengths (larger than 8 Å at our chosen parameters). To analyze the intensity distribution of all horizontal line cuts we use a simplified model to describe the structure of the PTB7:$PC_{71}BM$ films. This model assumes spherical-shaped scattering objects distributed over a one-dimensional para-crystal lattice within the frame of the distorted-wave Born approximation (DWBA) to determine the most prominent in-plane length scales.[44,46] From this model, form factors and structure factors as well as the size distributions can be extracted. The form factor is responsible for resolving the scattering objects, and the structure factor is associated with the spatial distribution of different scattering objects. Depending if volume or surface sensitive structure information is to be extracted, different numbers of form and structure factors are considered while modeling.

To detect the volume information (horizontal line cuts probed with short neutron wavelengths), two objects (R1 and R2) are required as well as two respective structure factors (D1 and D2). On the other hand, if surface information (horizontal line cuts probed with long neutron wavelengths) is of interest, only one object (R3) and structure factor (D3) are sufficient for modeling the corresponding curves. In Figure 6, the most prominent structural features of the PTB7:$PC_{71}BM$ BHJ active

DOI: 10.1021/am5079418
ACS Appl. Mater. Interfaces 2015, 7, 4641−4649

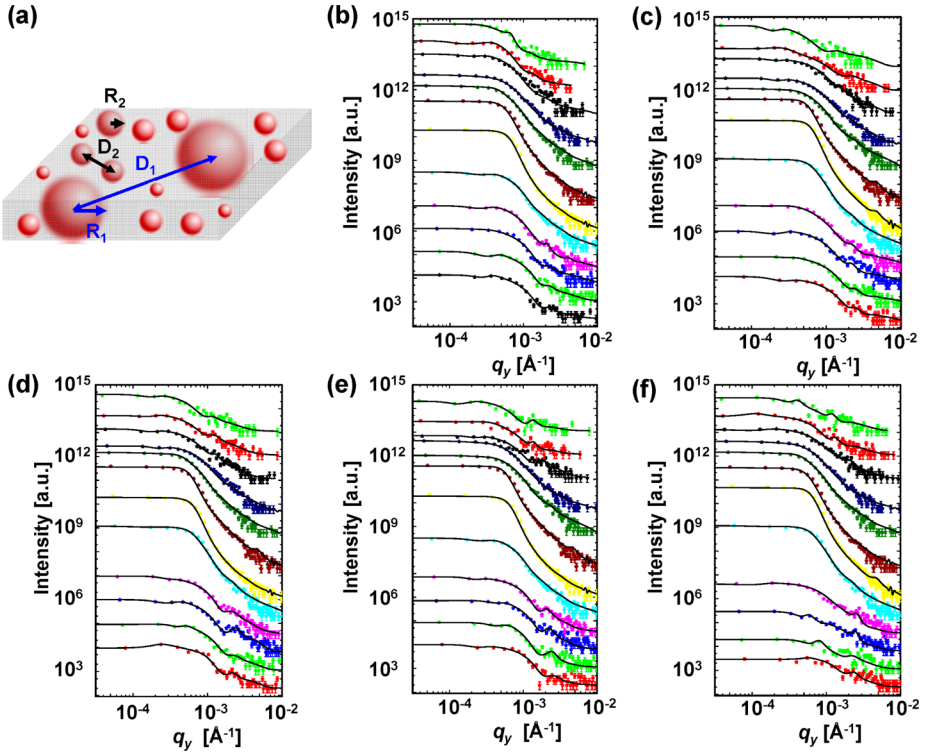

Figure 5. (a) Scheme of 1D paracrystal model within the framework of distorted wave Born approximation (DWBA) and logarithmic plots of the horizontal line cuts at the critical angles of the 2D TOF-GISANS data and the corresponding fits for PTB7:$PC_{71}BM$ films: (b) pristine film without any solvent treatment, (c) methanol-treated, (d) ethanol-treated, (e) 2-propanol-treated, and (f) 1-butanol-treated. The wavelength increases from 5.25 Å (bottom data points) to 10.75 Å (top data points) with an increment of 0.5 Å. The curves are shifted along the intensity axis for clarity of the presentation.

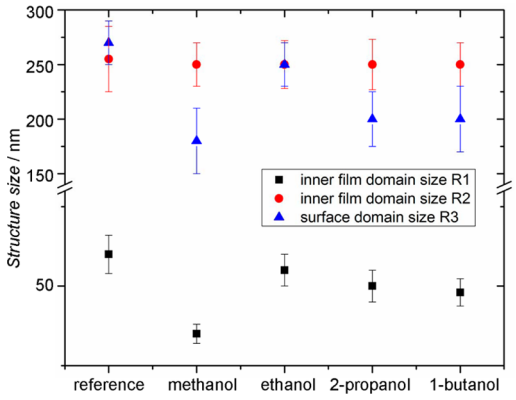

Figure 6. Most prominent structural features of PTB7:$PC_{71}BM$ BHJ active layers without and with post solvent treatment (methanol, ethanol, 2-propanol, and 1-butanol) as extracted from TOF-GISANS: two inner film domain sizes R1 (black squares), R2 (red circles), and one surface domain size R3 (blue triangle).

layers, without and with alcohol treatment (methanol, ethanol, 2-propanol, and 1-butanol), are shown. The two inner film domain sizes R1, R2, and the one surface domain size R3, as extracted from the fitting results, are plotted.

For both the pristine and solvent-treated PTB7:$PC_{71}BM$ BHJ films, the large inner domain sizes R2 (about 250 nm) and the distances between two adjacent domains D2 (not shown in the graph) remain rather constant. The surface domain sizes R3 and distance D3 are in a similar order. For all solvent-treated films a certain size decrease is found, and the smallest domain size is seen in case of methanol-treated films, agreeing with previous features of AFM error images. In contrast, more pronounced differences are observed for the small inner domain size R1, which evolves from (70 ± 6 nm) for the pristine PTB7:$PC_{71}BM$ BHJ films to smaller sizes in general for solvent-treated PTB7:$PC_{71}BM$ BHJ films. Among all the solvent-treated films, the one after methanol treatment exhibits the smallest inner lateral structures (35 ± 3 nm), which as a reasonable deduction will contribute to the improved J_{sc} and FF values since exciton splitting can be most efficient. Similar structural rearrangements induced by solvent treatment on a different low-bandgap polymer PBDTF-DFBO:$PC_{71}BM$ BHJ system were also observed by Wang et al. The authors claimed that the improved device performance originates from the formation of fiberlike interpenetrating morphologies and more balanced charge transport.[28] Therefore, it is suggested that solvent treatment improves the blend solubility and miscibility between PTB7 and $PC_{71}BM$. Particularly, the alcohol solvent with high volatility can take away residual DIO in the blend layer during evaporation,[19] hindering further diffusion of PCBM molecules,[47] and consequently produce an optimal interpenetrating structure for maximum PCE, as observed in the present investigation. In addition to the morphology changes found in the present study, it was also suggested by Zhang et al. that the modification of the interface between the active layer and PEDOT:PSS layer can be a reason for the efficiency enhancement induced by methanol treatment.[48] It was reported that methanol may also modify the work function of the PEDOT:PSS layer underneath the polymer:fullerene blend film, which contributes to improve the V_{oc} and consequently the device performance.[48,49] However, V_{oc} is also related to the morphology via charge recombination, and

DOI: 10.1021/am5079418
ACS Appl. Mater. Interfaces 2015, 7, 4641−4649

an optimized morphology of the active layer results in the highest V_{oc} values.

A sketch of the morphology of PTB7:$PC_{71}BM$ in the active layers without and with post solvent treatment is shown in Figure 7. The pristine film contains the largest average domains

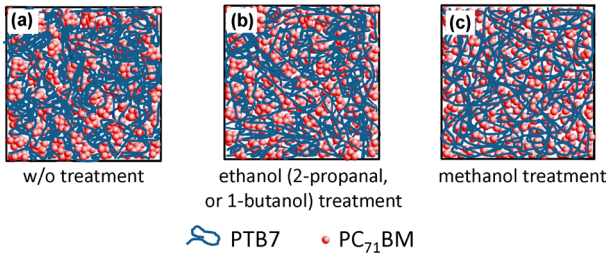

Figure 7. Representative schematic morphology of PTB7:$PC_{71}BM$ BHJ active layers (a) without solvent treatment, (b) with ethanol, 2-propanol, or 1-butanol treatment, and (c) with methanol treatment. Blue lines represent the polymer PTB7, and red spheres correspond to $PC_{71}BM$.

(Figure 7a), which due to alcohol treatment shrink to smaller length scales as shown in Figure 7b and c, evident by both AFM and TOF-GISANS data. Among all, methanol treatment gives rise to the smallest domain sizes (see Figure 7c), which cannot be explained by solubility of PTB7 or $PC_{71}BM$, since the four used alcohols have an extremely low solubility of the organic materials of the active layer. Therefore, we postulate that the shrinking of domain sizes for solvent-treated samples is caused by differences in the diffusion of the alcohol molecules and in the removal of residual DIO. As methanol has the smallest volume, it can penetrate best the whole active layer as compared with the other alcohols. Moreover, it can be removed best together with the residual solvent additive DIO from the blend layer due to its much higher volatility during evaporation,[19] thereby producing an optimal stable morphology for maximum PCE.[47] Ethanol is an exception, which might originate from an incompatibility between ethanol and certain materials used for the whole solar cell. In conclusion, the observed changes of the inner film morphology of the active layers are responsible for the enhanced PCE of the corresponding solar cells, evident by the improved J_{sc}, V_{oc}, and FF simultaneously.

4. CONCLUSION

This study further confirms that facile post treatment methods like alcohol treatment could become an efficient, economic strategy toward higher efficiency low-cost polymer solar cells superior to the laborious interlayer implementation. For the first time a systematic study of the effect of solvent treatment with a series of four different alcohol solvents on the polymer solar cell efficiency is reported. It is observed from our investigation that alcohol treatments with methanol, ethanol, 2-propanol, and 1-butanol all have a clear positive influence on the corresponding device performance. Devices with methanol treatment perform the best, and up to 25% enhancement of the PCE is obtained. The reason for this improvement is mainly studied in this investigation. From the absorption and optical characterization, homogeneous films with identical film thickness are observed for both pristine and alcohol-treated PTB7:$PC_{71}BM$ films. Thus, the performance enhancement is assumed to be caused by the morphological rearrangement. From the results obtained from AFM error images, slight structural modifications on the film surface are observed after solvent treatment: Phase separation structures with smaller domains are formed for all blend films with solvent treatment, and the film with methanol treatment gives rise to the smallest domain structures. From the TOF-GISANS measurements, we find an obvious change of the inner film morphology. The domain and structure sizes shrink for all the alcohol-treated samples, and the structural modifications for methanol-treated samples are the most pronounced among all the four tested alcohols.

As a result, it is proposed that the optimized film morphology improves the charge separation, transportation, and extraction effectively, which is evident by the simultaneous increase of J_{sc}, FF, and especially the V_{oc} introduced by alcohol treatment. Moreover, among the four alcohol solvents, methanol appears to be the most effective, possibly due to its smallest size and highest penetration rate through the active layer, resulting in optimized film mophology and consequently highest PCE. Taking into account the success of solvent treatment on other material combinations such as the well-studied P3HT:$PC_{60}BM$ BHJ system,[22,24,37] it is positively suggested that alcohol treatment can be widely applied to other polymer:fullerene systems as an easy and efficient method to greatly improve the device performance.

■ ASSOCIATED CONTENT

Supporting Information

Corresponding optical microscopy images, AFM topography images for pristine and solvent-treated PTB7:$PC_{71}BM$ BHJ films (Figure S1 and Figure S2, respectively); vertical line cuts of 2D TOF-GISANS data (Figure S3); extracted wavelength dependence of the Yoneda peak position (Figure S4).This material is available free of charge via the Internet at http://pubs.acs.org.

■ AUTHOR INFORMATION

Corresponding Author

*Fax: +49 (0)89 289 12473. Tel.: +49 (0)89 289 12451. E-mail: muellerb@ph.tum.de.

Author Contributions

All authors have given approval to the final version of the manuscript.

Notes

The authors declare no competing financial interest.

■ ACKNOWLEDGMENTS

The financial support from TUM.solar in the frame of the Bavarian Collaborative Research Project "Solar technologies go Hybrid" (SolTec), the GreenTech Initiative (Interface Science for Photovoltaics—ISPV) of the EuroTech Universities, the German Research Foundation (DFG) in the "SPP1355: Elementary processes of organic photovoltaics", and the Nanosystems Initiative Munich (NIM) is greatly acknowledged. B.C. thanks the Erasmus Mundus "MaMaSELF" program. W.W. thanks the funding from China Scholarship Council (CSC).

■ ABBREVIATIONS

AFM, atomic force microscopy; BHJ, bulk heterojunction; DIO, 1,8-diiodooctane; ITO, indium tin oxide; PEDOT:PSS, poly(3,4-ethylenedioxythiophene):poly(styrenesulfonate); $PC_{71}BM$, [6,6]-phenyl-C71-butyric acid methyl ester; PTB7,

DOI: 10.1021/am5079418
ACS Appl. Mater. Interfaces 2015, 7, 4641−4649

poly[[4,8-bis[(2-ethylhexyl)oxy]benzo[1,2-*b*:4,5-*b*′]-dithiophene-2,6-diyl][3-fluoro-2-[(2-ethylhexyl)carbonyl]-thieno[3,4-*b*]thiophenediyl]]; TOF-GISANS, time-of-flight-grazing incidence small-angle neutron scattering; PSCs, polymer solar cells; PCE, power conversion efficiency

REFERENCES

(1) Yu, G.; Gao, J.; Hummelen, J. C.; Wudl, F.; Heeger, A. J. Polymer Photovoltaic Cells: Enhanced Efficiencies via a Network of Internal Donor−Acceptor Heterojunctions. *Science* **1995**, *270*, 1789−1791.

(2) Granström, M.; Petritsch, K.; Arias, A. C.; Lux, A.; Andersson, M. R.; Friend, R. H. Laminated Fabrication of Polymeric Photovoltaic Diodes. *Nature* **1998**, *395*, 257−260.

(3) Dennler, G.; Scharber, M. C.; Ameri, T.; Denk, P.; Forberich, K.; Waldauf, C.; Brabec, C. J. Design Rules for Donors in Bulk-Heterojunction Tandem Solar Cells Towards 15% Energy-Conversion Efficiency. *Adv. Mater.* **2008**, *20*, 579−583.

(4) Zhou, H.; Yang, L.; You, W. Rational Design of High Performance Conjugated Polymers for Organic Solar Cells. *Macromolecules* **2012**, *45*, 607−632.

(5) Peters, C. H.; Sachs-Quintana, I. T.; Kastrop, J. P.; Beaupré, S.; Leclerc, M.; McGehee, M. D. High Efficiency Polymer Solar Cells with Long Operating Lifetimes. *Adv. Energy Mater.* **2011**, *1*, 491−494.

(6) McNeill, C. R.; Gowrisanker, S.; Halls, J. J. M.; Laird, D.; Jia, S.; Willams, S. P. Polymer−Fullerene Bulk-Heterojunction Solar Cells. *Adv. Mater.* **2010**, *22*, 3839−3856.

(7) Blakers, A.; Zin, N.; McIntosh, K. R.; Fong, K. High Efficiency Silicon Solar Cells. *Energy Procedia* **2013**, *33*, 1−10.

(8) Lipomi, D. J.; Tee, B. C.-K.; Vosgueritchian, M.; Bao, Z. Stretchable Organic Solar Cells. *Adv. Mater.* **2011**, *23*, 1771−1775.

(9) Darling, S. B.; You, F. The Case for Organic Photovoltaics. *RSC Adv.* **2013**, *3*, 17633−17648.

(10) Li, X.-G.; Huang, M.-R.; Duan, W.; Yang, Y.-L. Novel Multifunctional Polymers from Aromatic Diamines by Oxidative Polymerizations. *Chem. Rev.* **2002**, *102*, 2925−3030.

(11) Guo, S.; Ning, J.; Körstgens, V.; Yao, Y.; Herzig, E. M.; Roth, S. V.; Müller-Buschbaum, P. The Effect of Fluorination in Manipulating the Nanomorphology in PTB7:$PC_{71}BM$ Bulk Heterojunction Systems. *Adv. Energy Mater.* **2014**, DOI: 10.1002/aenm.201401315.

(12) Liao, H.-C.; Ho, C.-C.; Chang, C.-Y.; Jao, M.-H.; Darling, S. B.; Su, W.-F. Additives for Morphology Control in High-Efficiency Organic Solar Cells. *Mater. Today* **2013**, *16*, 326−336.

(13) He, Z.; Zhong, C.; Su, S.; Xu, M.; Wu, H.; Cao, Y. Enhanced Power-Conversion Efficiency in Polymer Solar Cells Using an Inverted Device Structure. *Nat. Photon.* **2012**, *6*, 591−595.

(14) Wang, T.; Pearson, A. J.; Lidzey, D. G. Correlating Molecular Morphology with Optoelectronic Function in Solar Cells Based on Low Band-Gap Copolymer:Fullerene Blends. *J. Mater. Chem. C* **2013**, *1*, 7266−7293.

(15) Green, M. A.; Emery, K.; Hishikawa, Y.; Warta, W.; Dunlop, E. D. Solar Cell Efficiency Tables (version 43). *Prog. Photovoltaics* **2014**, *22*, 1−9.

(16) Lee, J. K.; Ma, W. L.; Brabec, C. J.; Yuen, J.; Moon, J. S.; Kim, J. Y.; Lee, K.; Bazan, G. C.; Heeger, A. J. Processing Additives for Improved Efficiency from Bulk Heterojunction Solar Cells. *J. Am. Chem. Soc.* **2008**, *130*, 3619−3623.

(17) Peet, J.; Kim, J. Y.; Coates, N. E.; Ma, W. L.; Moses, D.; Heeger, A. J.; Bazan, G. C. Efficiency Enhancement in Low-Bandgap Polymer Solar Cells by Processing with Alkane Dithiols. *Nat. Mater.* **2007**, *6*, 497.

(18) Liang, Y.; Xu, Z.; Xia, J.; Tsai, S.-T.; Wu, Y.; Li, G.; Ray, C.; Yu, L. For the Bright Future—Bulk Heterojunction Polymer Solar Cells with Power Conversion Efficiency of 7.4%. *Adv. Funct. Mater.* **2010**, *22*, E135−E138.

(19) Ye, L.; Jing, Y.; Guo, X.; Sun, H.; Zhang, S.; Zhang, M.; Huo, L.; Hou, J. Remove the Residual Additives toward Enhanced Efficiency with Higher Reproducibility in Polymer Solar Cells. *J. Phys. Chem. C* **2013**, *117*, 14920−14928.

(20) Zhou, H.; Zhang, Y.; Seifter, J.; Collins, S. D.; Luo, C.; Bazan, G. C.; Nguyen, T.-Q.; Heeger, A. J. High-Efficiency Polymer Solar Cells Enhanced by Solvent Treatment. *Adv. Mater.* **2013**, *25*, 1646−1652.

(21) He, Z.; Zhong, C.; Huang, X.; Wong, W.-Y.; Wu, H.; Chen, L.; Su, S.; Cao, Y. Simultaneous Enhancement of Open-Circuit Voltage, Short-Circuit Current Density, and Fill Factor in Polymer Solar Cells. *Adv. Mater.* **2011**, *23*, 4636−4643.

(22) Liu, X.; Wen, W.; Bazan, G. C. Post-Deposition Treatment of an Arylated-Carbazole Conjugated Polymer for Solar Cell Fabrication. *Adv. Mater.* **2012**, *24*, 4505−4510.

(23) Gu, C.; Chen, Y.; Zhang, Z.; Xue, S.; Sun, S.; Zhong, C.; Zhang, H.; Lv, Y.; Li, F.; Huang, F.; Ma, Y. Achieving High Efficiency of PTB7-Based Polymer Solar Cells via Integrated Optimization of Both Anode and Cathode Interlayers. *Adv. Energy Mater.* **2014**, DOI: 10.1002/aenm.201301771.

(24) Li, H.; Tang, H.; Li, L.; Xu, W.; Zhao, X.; Yang, X. Solvent-Soaking Treatment Induced Morphology Evolution in P3HT/PCBM Composite Films. *J. Mater. Chem.* **2011**, *21*, 6563−6568.

(25) Ruderer, M. A.; Müller-Buschbaum, P. Morphology of Polymer-Based Bulk Heterojunction Films for Organic Photovoltaics. *Soft Matter* **2011**, *7*, 5482−5493.

(26) Chen, W.; Nikiforov, M. P.; Darling, S. B. Morphology Characterization in Organic and Hybrid Solar Cells. *Energy Environ. Sci.* **2012**, *5*, 8045−8074.

(27) Liu, F.; Gu, Y.; Jung, J. W.; Jo, W. H.; Russell, T. P. On the Morphology of Polymer-based Photovoltaics. *J. Polym. Sci., Part B: Polym. Phys.* **2012**, *50*, 1018−1044.

(28) Wang, Y.; Liu, Y.; Chen, S.; Peng, R.; Ge, Z. Significant Enhancement of Polymer Solar Cell Performance via Side-Chain Engineering and Simple Solvent Treatment. *Chem. Mater.* **2013**, *25*, 3196−3204.

(29) Torikai, N.; Noda, I.; Karim, A.; Satija, S. K.; Han, C. C.; Matsushita, Y.; Kawakatsu, T. Neutron Reflection Studies on Segment Distribution of Block Chains in Lamellar Microphase-Separated Structures. *Macromolecules* **1997**, *30*, 2907−2914.

(30) Dalgliesh, R. Application of Off-Specular Scattering of X-rays and Neutrons to the Study of Soft Matter. *Curr. Opin. Colloid Interface Sci.* **2002**, *7*, 244−248.

(31) Smilgies, D.-M.; Busch, P.; Papadakis, C. M.; Posselt, D. Characterization of Polymer Thin Films with Small-Angle X-ray Scattering under Grazing Incidence (GISAXS). *Synchrotron Rad. News* **2002**, *15*, 35−42.

(32) Staniec, P. A.; Parnell, A. J.; Dunbar, A. D. F.; Yi, H.; Pearson, A. J.; Wang, T.; Hopkinson, P. E.; Kinane, C.; Dalgliesh, R. M.; Donald, A. M.; Ryan, A. J.; Iraqi, A.; Jones, R. A. L.; Lidzey, D. G. The Nanoscale Morphology of a PCDTBT:PCBM Photovoltaic Blend. *Adv. Energy Mater.* **2011**, *1*, 499−504.

(33) Korolkov, D.; Busch, P.; Willner, L.; Kentzinger, E.; Rücker, U.; Paul, A.; Frielinghaus, H.; Brückel, T. Analysis of Randomly Oriented Structures by Grazing-Incidence Small-Angle Neutron Scattering. *J. Appl. Crystallogr.* **2012**, *45*, 245−254.

(34) Müller-Buschbaum, P. Grazing Incidence Small-Angle Neutron Scattering: Challenges and Possibilities. *Polym. J. (Tokyo, Jpn.)* **2013**, *45*, 34−42.

(35) Ruderer, M. A.; Meier, R.; Porcar, L.; Cubitt, R.; Müller-Buschbaum, P. Phase Separation and Molecular Intermixing in Polymer−Fullerene Bulk Heterojunction Thin Films. *J. Phys. Chem. Lett.* **2012**, *3*, 683−688.

(36) Kingsley, J. W.; Marchisio, P. P.; Yi, H.; Iraqi, A.; Kinane, C. J.; Langridge, S.; Thompson, R. L.; Cadby, A. J.; Pearson, A. J.; Lidzey, D. G.; Jones, R. A. L.; Parnell, A. J. Molecular Weight Dependent Vertical Composition Profiles of PCDTBT:$PC_{71}BM$ Blends for Organic Photovoltaics. *Sci. Rep.* **2014**, *4*, 5286−1−5286−7.

(37) Ruderer, M. A.; Guo, S.; Meier, R.; Chiang, H.-Y.; Körstgens, V.; Wiedersich, J.; Perlich, J.; Roth, S. V.; Müller-Buschbaum, P. Solvent-Induced Morphology in Polymer-Based Systems for Organic Photovoltaics. *Adv. Funct. Mater.* **2011**, *21*, 3382−3391.

DOI: 10.1021/am5079418
ACS Appl. Mater. Interfaces 2015, 7, 4641−4649

(38) Müller-Buschbaum, P. The Active Layer Morphology of Organic Solar Cells Probed with Grazing Incidence Scattering Techniques. *Adv. Mater.* **2014**, *26*, 7692−7709.
(39) Rivnay, J.; Mannsfeld, S. C. B.; Miller, C. E.; Salleo, A.; Toney, M. F. Quantitative Determination of Organic Semiconductor Microstructure from the Molecular to Device Scale. *Chem. Rev.* **2012**, *112*, 5488−5519.
(40) Müller-Buschbaum, P.; Gutmann, J. S.; Cubitt, R.; Stamm, M. Probing the in-Plane Composition of Thin Polymer Films with Grazing-Incidence Small-Angle Neutron Scattering and Atomic Force Microscopy. *Colloid Polym. Sci.* **1999**, *277*, 1193−1199.
(41) Müller-Buschbaum, P.; Kaune, G.; Haese-Seiller, M.; Moulin, J.-F. Morphology Determination of Defect-rich Diblock Copolymer Films with Time-of-Flight Grazing Incidence Small Angle Neutron Scattering. *J. Appl. Crystallogr.* **2014**, *47*, 1228−1237.
(42) Müller-Buschbaum, P. Influence of Surface Cleaning on Dewetting of Thin Polystyrene Films. *Eur. Phys. J. E: Soft Matter Biol. Phys.* **2003**, *12*, 443−448.
(43) Müller-Buschbaum, P.; Metwalli, E.; Moulin, J.-F.; Kudryashov, V.; Haese-Seiller, M.; Kampmann, R. Time-of Flight Grazing Incidence Small Angle Neutron Scattering—A Novel Scattering Technique for the Investigation of Nanostructured Polymer Films. *Euro. Phys. J.: Spec. Top.* **2009**, *167*, 107−112.
(44) Müller-Buschbaum, P. Grazing Incidence Small-Angle X-ray Scattering—An Advanced Scattering Technique for the Investigation of Nanostructured Polymer Films. *Anal. Bioanal. Chem.* **2003**, *376*, 3−10.
(45) Dosch, H. In *Critical Phenomena at Surface and Interfaces: Evanescent X-ray and Neutron Scattering*; Springer-Verlag: Heidelberg, Germany, 1992; Chapter 2, pp 6−31.
(46) Müller-Buschbaum, P. In *Applications of Synchrotron Light to Scattering and Diffraction in Materials and Life Sciences*; Ezquerra, T. A., Garcia-Gutierrez, M. C., Nogales, A., Gomez, M., Eds.; Springer: Berlin, Germany, 2009; Chapter 3, pp 61−89.
(47) Chang, L.; Lademann, H. W. A.; Bonekamp, J.-B.; Meerholz, K.; Moulé, A. J. Effect of Trace Solvent on the Morphology of P3HT:PCBM Bulk Heterojunction Solar Cells. *Adv. Energy Mater.* **2011**, *21*, 1779−1787.
(48) Zhang, K.; Hu, Z.; Duan, C.; Ying, L.; Huang, F.; Cao, Y. The Effect of Methanol Treatment on the Performance of Polymer Solar Cells. *Nanotechnology* **2013**, *24*, 484003−1−484003−7.
(49) Synooka, O.; Kretschmer, F.; Hager, M. D.; Himmerlich, M.; Krischok, S.; Gehrig, D.; Laquai, F.; Schubert, U. S.; Gobsch, G.; Hoppe, H. Modification of the Active Layer/PEDOT:PSS Interface by Solvent Additives Resulting in Improvement of the Performance of Organic Solar Cells. *ACS Appl. Mater. Interfaces* **2014**, *6*, 11068−11081.

DOI: 10.1021/am5079418
ACS Appl. Mater. Interfaces 2015, 7, 4641−4649